Supplementary Information

Atmospheric-moisture-driven evaporative cooling and concurrent hydrovoltaic energy harvesting in photovoltaic panels

Sunmiao Fang, Yuxuan Huang, Saichao Dang, Khalid Hazazi, Yue Cao, Jiachen Wang, Pingfan Wu, Stefaan De Wolf, Hussam Qasem, Qiaoqiang Gan*

*Corresponding author: qiaoqiang.gan@kaust.edu.sa.

The PDF file includes:

Figures S1 to S32
Tables S1 to S4
References

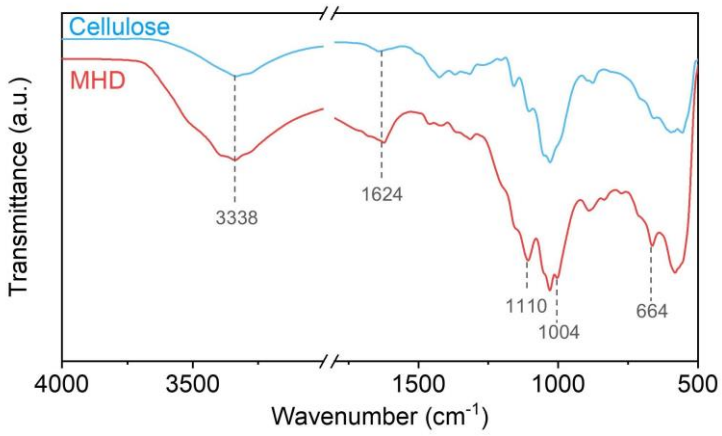

Figure S1. Fourier transform infrared spectra of the pristine cellulose (blue) and MHD (red). The newly appeared peaks at 1110, 1004, and 664 cm^{-1} in the MHD are attributed to the asymmetrical and symmetrical stretching vibrations of S=O and the bending vibration of S–O–H, indicating successful incorporation of H_2SO_4 and PSSA.[1] The enhanced peaks at 3338 and 1624 cm^{-1}, corresponding to stretching and bending vibration of O–H bonds, are associated with added sulfonic acid groups and adsorbed water molecules in the MHD.[2]

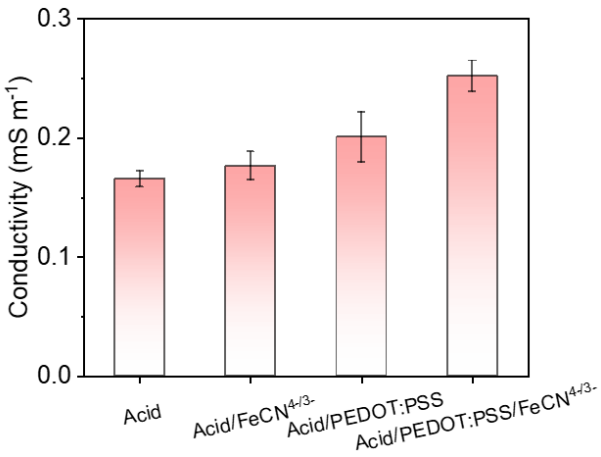

Figure S2. Electrical conductivity of cellulose composites with varying compositions. The electrical conductivity of the membrane is significantly enhanced by the incorporation of conductive additives. The results show a clear hierarchy of conductivity: bare acid treatment < acid + $K_3[Fe(CN)_6]/K_4[Fe(CN)_6]$ < acid + PEDOT:PSS < acid + PEDOT:PSS + $K_3[Fe(CN)_6]/K_4[Fe(CN)_6]$, highlighting the synergistic effect of these components.

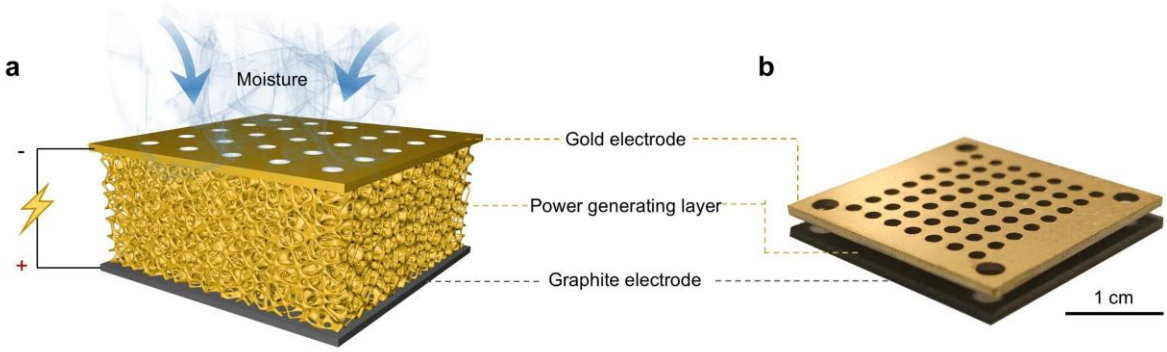

Figure S3. Structure of the MHD. (a) Schematic illustration and (b) photograph of the MHD, consisting of a top gold electrode, a power-generating layer, and a bottom graphite electrode. The porous top electrode facilitates moisture adsorption by the power-generating layer from the ambient environment.

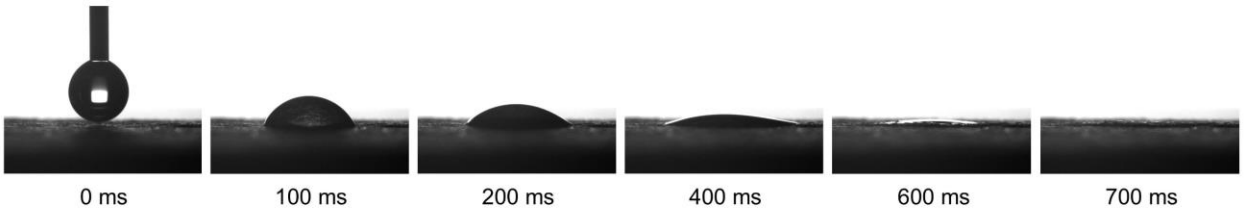

Figure S4. Water contact angle of the MHD. A water droplet (4 μL) rapidly infiltrates into the power-generating layer within 700 ms, indicating the high hydrophilicity of the membrane.

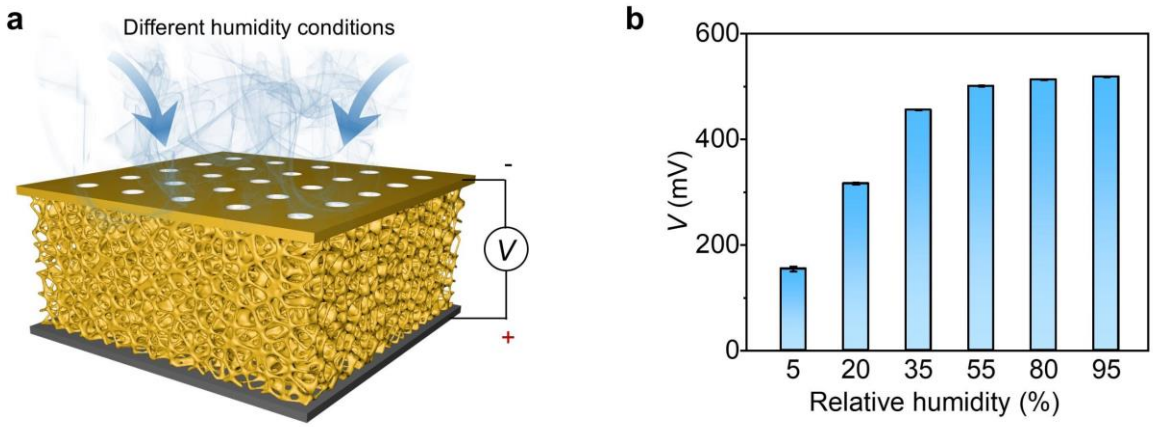

Figure S5. Output voltage of the MHD. (a) Schematic illustration of the experimental set-up for voltage measurement. The bottom and top electrodes of the MHD are connected to the positive and negative terminals of a source meter, respectively. The open-circuit voltage is recorded under zero applied current (I = 0 mA). (b) Output voltage as a function of ambient relative humidity (RH). The voltage increases with RH, highlighting the humidity-dependent energy-harvesting capability of the device.

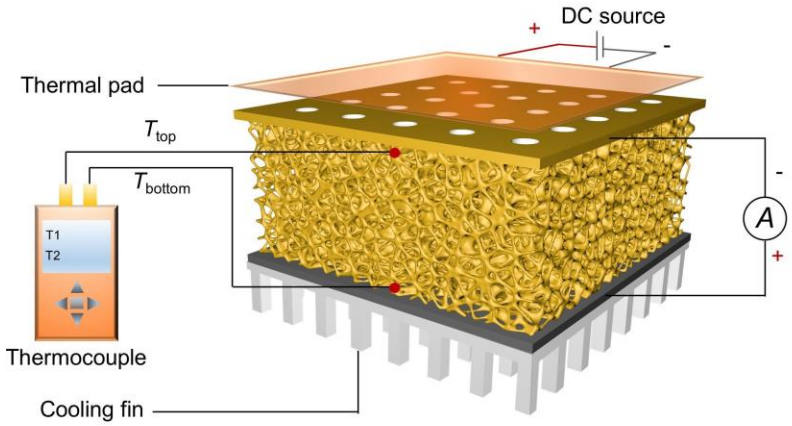

Figure S6. Experimental set-up for measuring the effect of a temperature gradient on power generation. The top surface of the MHD is heated with a thermal pad, while the bottom surface is connected to a cooling fin. The temperatures of the top (T_{top}) and bottom surfaces (T_{bottom}) of the power-generating layer are recorded using a multichannel thermocouple thermometer. The temperature difference (ΔT) is defined as $T_{top} - T_{bottom}$.

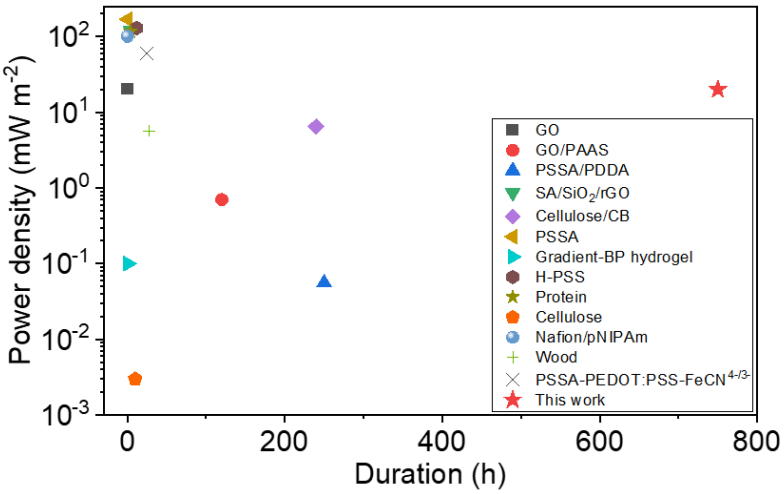

Figure S7. Comparison of output power density and duration of the MHD in this work with previously reported studies. The present device exhibits comparable power density to state-of-the-art MHD systems and demonstrates significantly longer operational duration (up to 30 days), representing a key performance advantage for practical deployment. Detailed data are provided in Table S1.

Figure S8. Photographs of the pristine cellulose and the MHD immersed in methyl orange/water solution (0.1% w/v in water). The methyl orange solution is a typical pH indicator, changing from orange to red when the pH changes from 4.4 to 3.1 For the MHD, the solution color changes from orange to red, indicating the presence of acid groups (e.g. sulfuric and sulfonic acid groups) that release abundant H^+ ions upon contact with water. In contrast, pristine cellulose shows limited H^+ dissociated from hydroxyl groups.

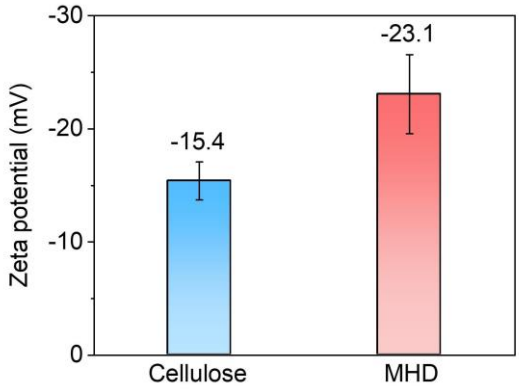

Figure S9. Zeta potentials of the pristine cellulose (blue) and MHD (red). The more negative zeta potential of the MHD indicates that its surface channels are more negatively charged compared with pristine cellulose.

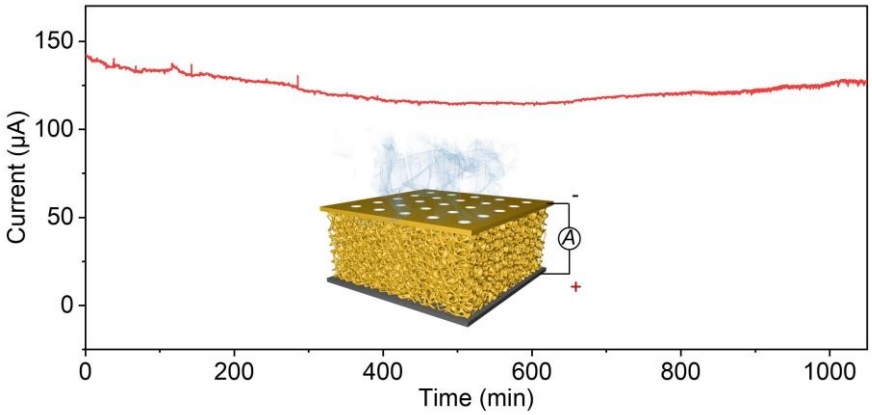

Figure S10. Long-time current measurement of the MHD under ambient conditions (20 °C, 60% RH). The inset shows a schematic of the experimental setup where the bottom and top electrodes of the MHD are connected to the positive and negative terminals of a source meter. The short-circuit current is measured under zero applied current ($V = 0$). The effective area of the MHD is approximately 4 cm^2.

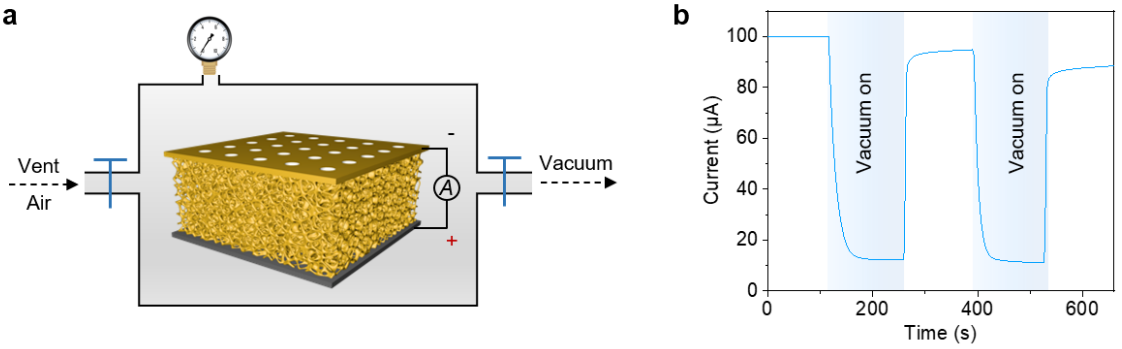

Figure S11. Output of the MHD under alternating humidity and vacuum conditions. (a) Schematic of the vacuum set-up. (b) Stepwise current output under alternating humidity and vacuum conditions. Shaded regions indicate vacuum periods.

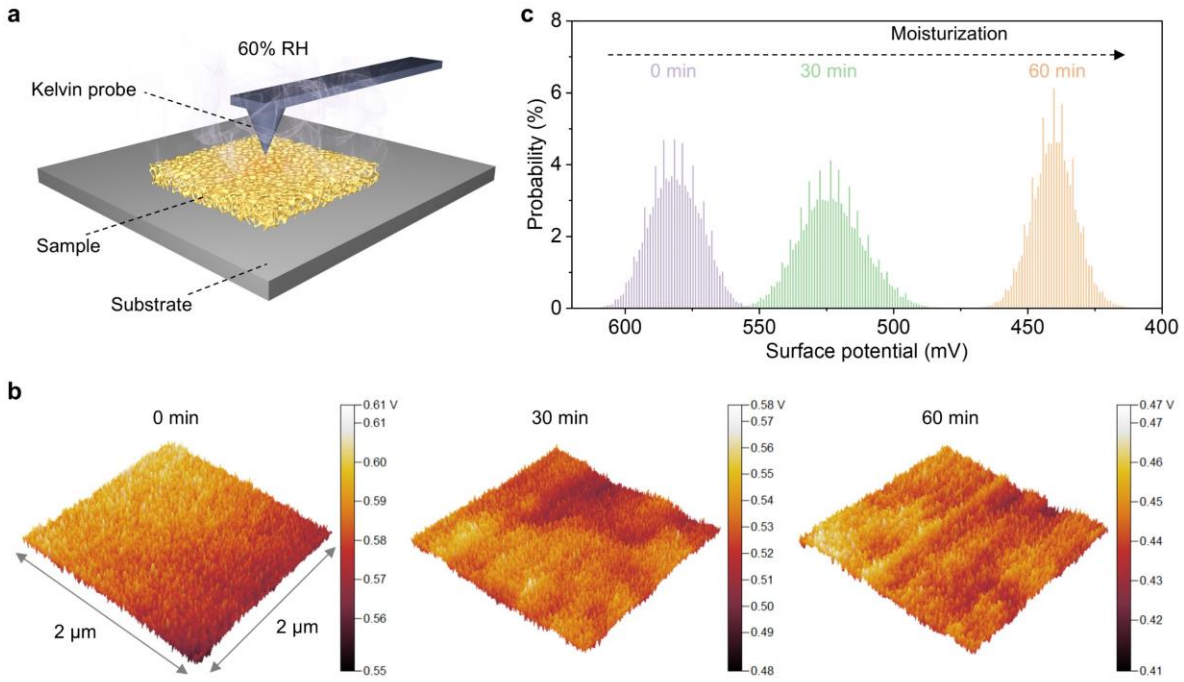

Figure S12. Kelvin probe force microscopy (KPFM) characterization of the MHD. (a) Surface potential measurements of the MHD are performed with the top surface exposed to the ambient environment (60% RH) over 0–60 min. (b) Surface potential maps acquired after 0, 30, and 60 min of moisture absorption over a 2 × 2 μm^2 area. (c) Evolution of surface potential distribution over time, showing a progressive reduction after moisture uptake.

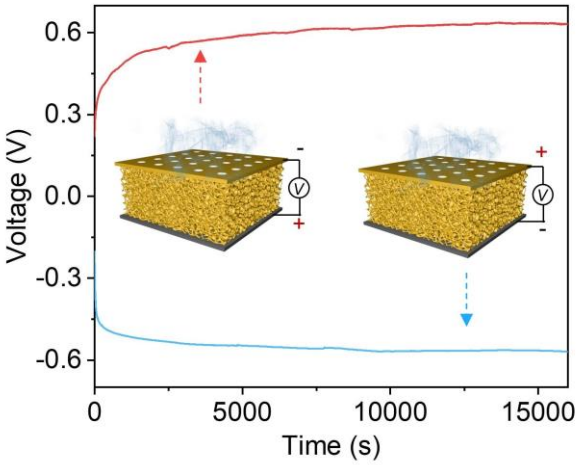

Figure S13. Voltage measurement of the MHD in forward and reverse directions. The measured reversed voltage upon swapping the electrodes indicates that the bottom end of the MHD acts as the anode, while the top end serves as the cathode.

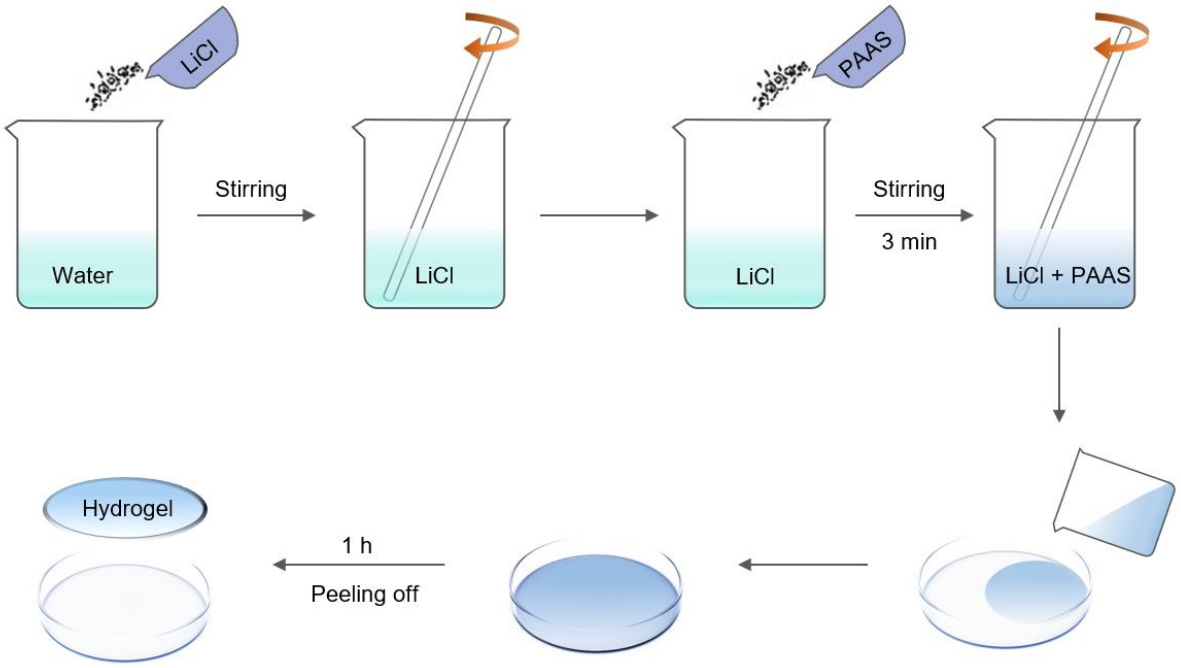

Figure S14. Fabrication process of the PAAS/LiCl hydrogel. LiCl is first dissolved in deionized water under vigorous stirring. After cooling to room temperature, PAAS powder is added to the LiCl solution and stirred for 3 min. The mixture is then poured into a culture dish and left to stand for 1 h. Finally, the PAAS/LiCl hydrogel is peeled off. Detailed fabrication procedures are provided in the Experimental section.

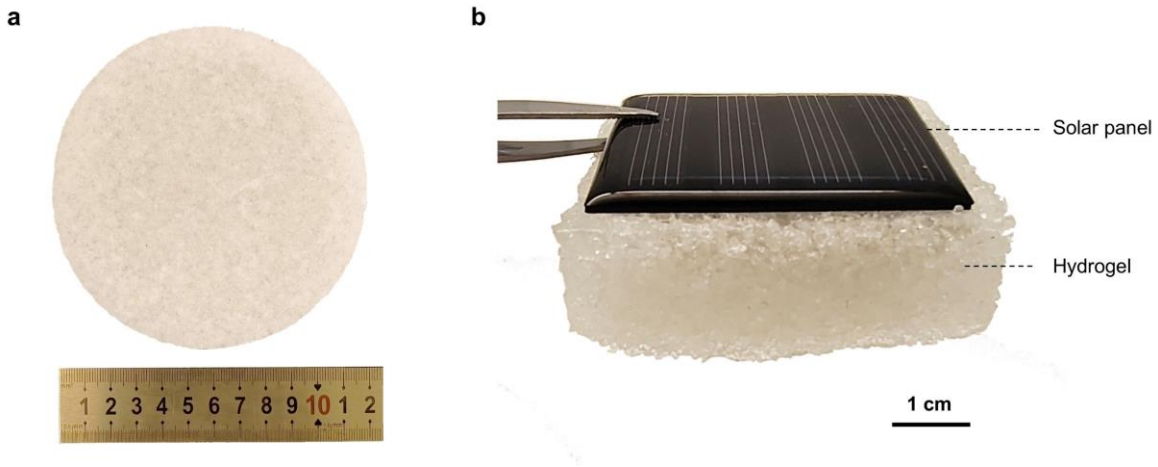

Figure S15. Photographs of the PAAS/LiCl hydrogel. (**a**) Top-view photograph of the hydrogel. (**b**) Cross-sectional photograph of the hydrogel attached to the backside of a PV panel.

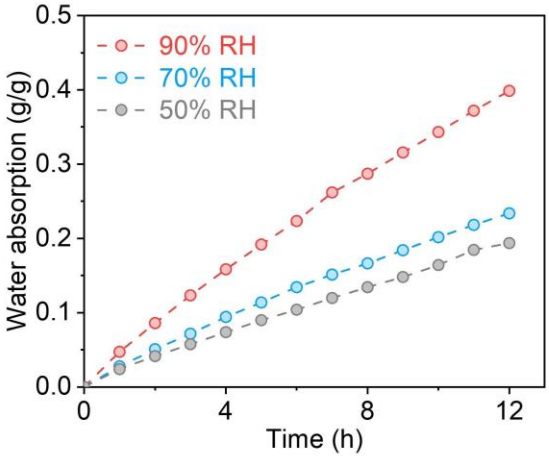

Figure S16. Water uptake of the PAAS/LiCl hydrogel under different relative humidities over 12 h at 20 °C. The pre-dried hydrogel exhibits a water uptake of approximately 0.19 g g^{-1} under 50% RH. The sample can absorb more water as the ambient humidity further increases.

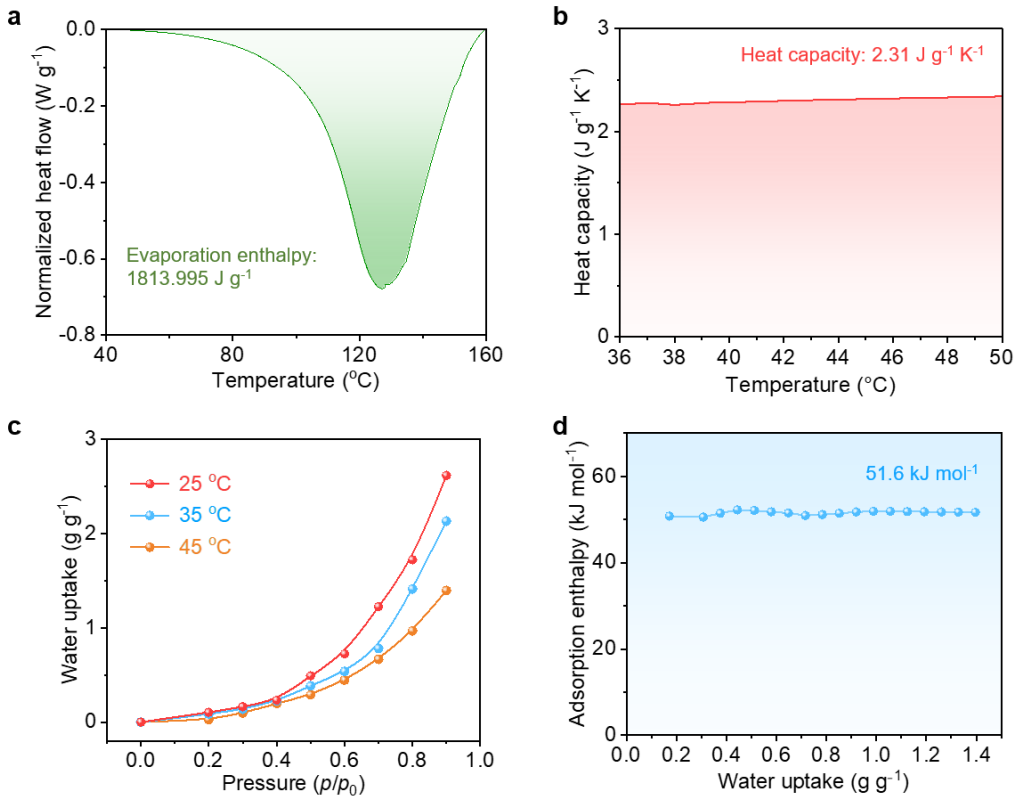

Figure S17. Thermophysical properties of the PAAS/LiCl hydrogel. (a) Differential scanning calorimetry curve showing the endothermic peak associated with water evaporation, corresponding to an evaporation enthalpy of ~1814 J g^{-1}. (b) Temperature-dependent specific heat capacity of the hydrogel, with an average value of ~2.31 J g^{-1} K^{-1} between 35 and 50 °C. (c) Water vapor adsorption isotherms measured at 25, 35, and 45 °C. (d) Adsorption enthalpy calculated from the isotherms using the Clausius–Clapeyron relation (~51.6 kJ mol^{-1}).[3]

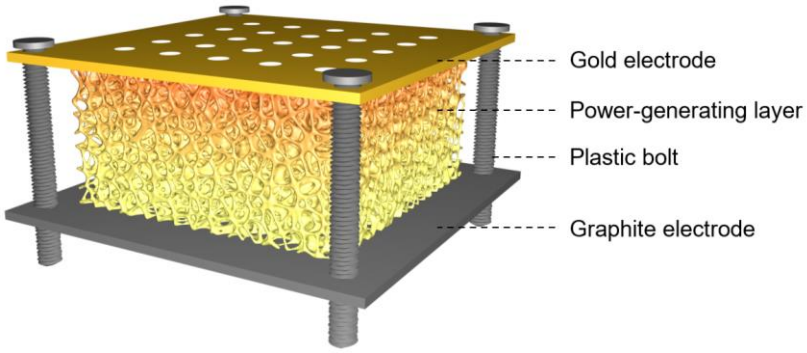

Figure S18. Schematic of the MHD device structure. The device consists of a top gold electrode, a moisture power-generating layer, and a bottom graphite electrode, which are fastened together with plastic bolts at the four corners without adhesive.

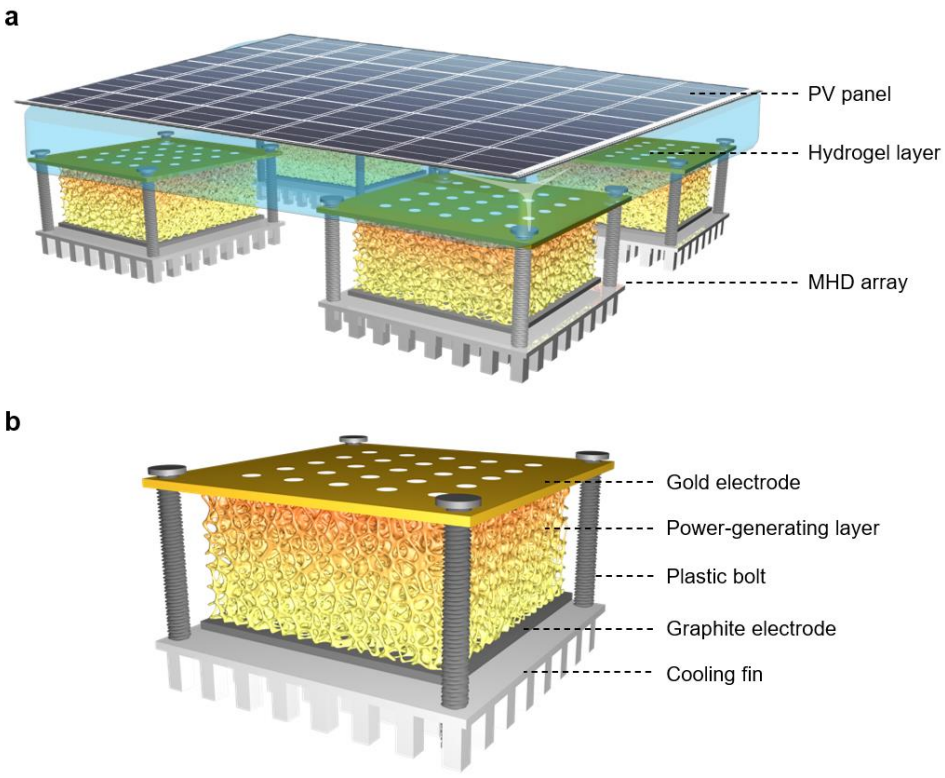

Figure S19. Schematic of the integrated PV–hydrovoltaic system. (a) The hydrogel layer is attached to the back surface of the PV panel, followed by the MHD array coupled with the cooling fin. (b) A single MHD unit is coupled with the cooling fin using the same set of bolts, ensuring tight interlayer contact and structural stability.

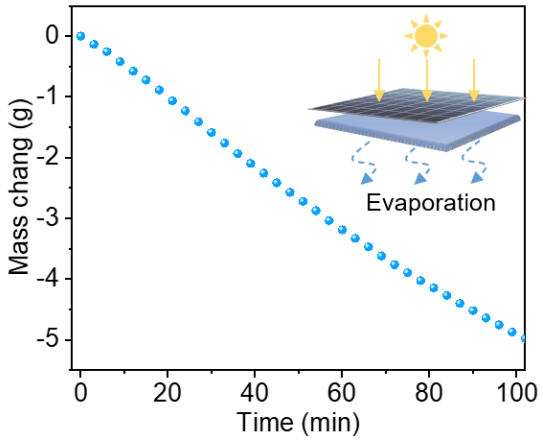

Figure S20. Time-dependent mass loss of the hydrogel cooling layer mounted to the backside of the PV panel under one-sun illumination. The surface area of the hydrogel is 49 cm^2. Based on the measured mass loss, the average cooling power falls in the range of 302–408 W m^{-2}, corresponding to calculations based on the hydrogel-specific evaporation enthalpy (1814 J g^{-1}) and the latent heat of liquid water (2450 J g^{-1}), respectively.[4]

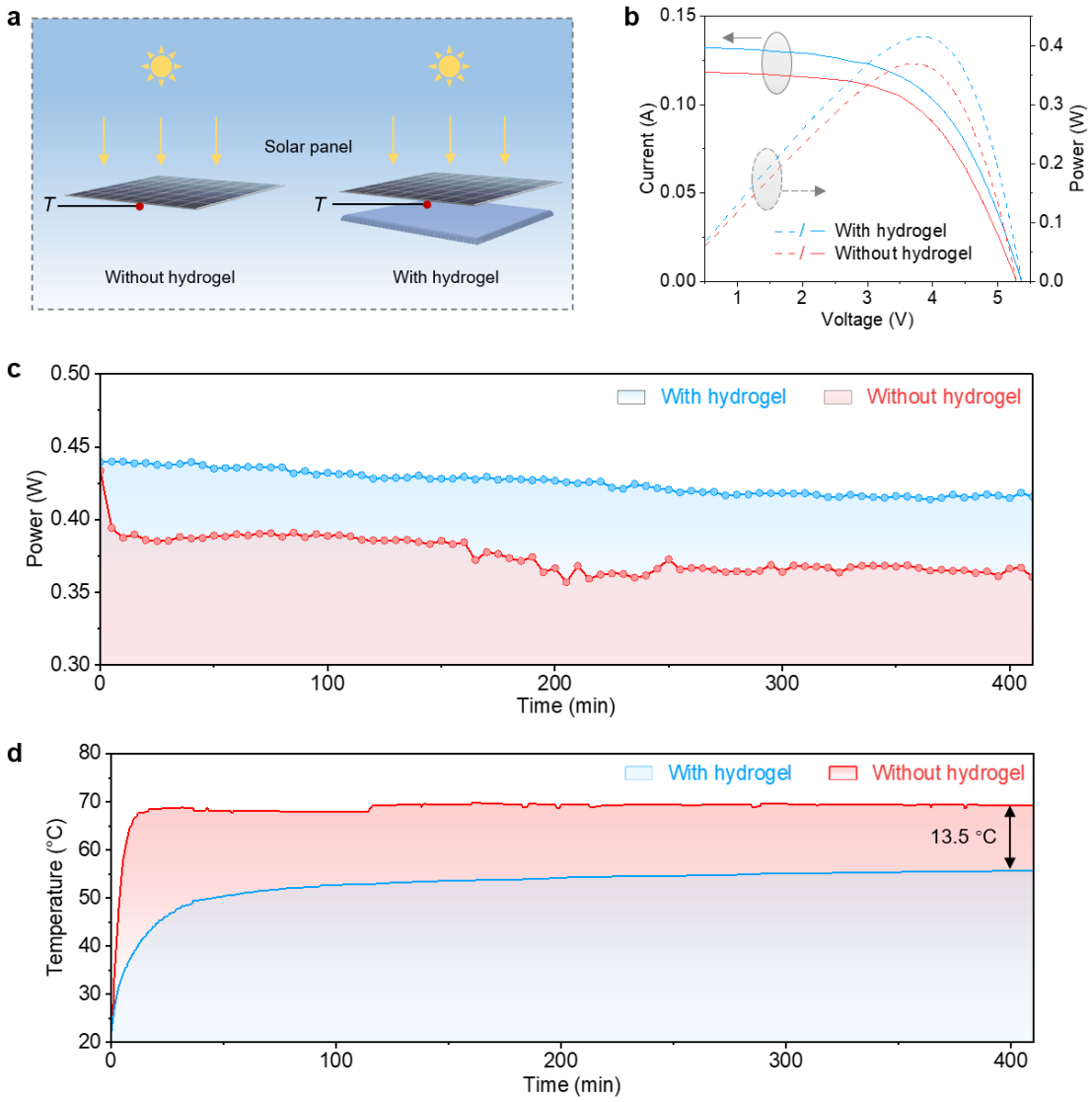

Figure S21. Long-time output performance of the PV panel with and without the hydrogel cooling layer. (a) Schematic of the PV panel with (left) and without the hydrogel cooling layer (right) under solar illumination. (b) Current–voltage curves (solid lines) output power (dashed lines) of the PV panel with (blue) and without the hydrogel cooling layer (red) after 400 min of one-sun illumination. (c) Peak output power of the PV panel versus time with (blue circles) and without the hydrogel cooling layer (red circles) under one-sun illumination. (d) Temperature of the PV panel versus time with (blue curve) and without the hydrogel cooling layer (red curve) under one-sun illumination. After 400 min of one-sun illumination, the temperature of the PV panel with the hydrogel cooling layer is approximately 13.5 °C lower than that of without hydrogel.

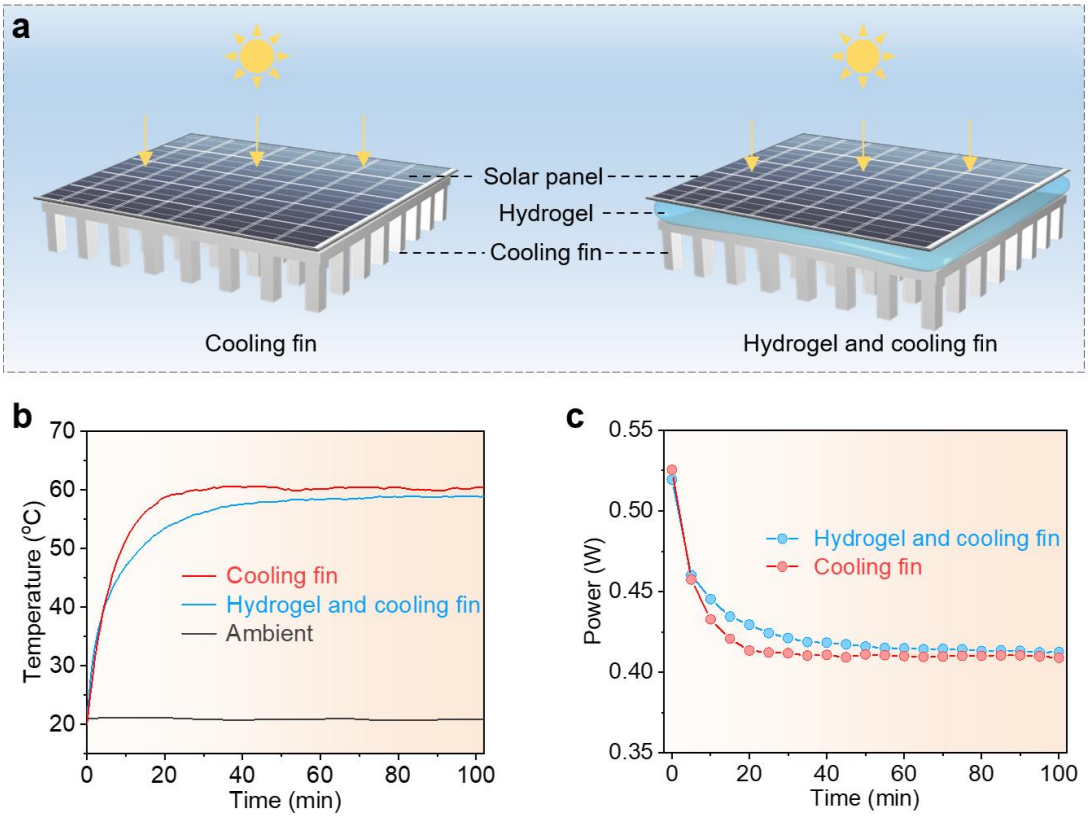

Figure S22. Thermal and electrical performance of the PV panel with different cooling strategies. (a) Schematic illustration of the PV panel equipped with a cooling fin (left) and with both hydrogel and cooling fin (right). (b) Surface temperature evolution of the PV panel with a cooling fin (red) and with both hydrogel and cooling fin (blue) under one-sun illumination (ambient temperature ≈ 20.6 °C). (c) Corresponding output power variation under solar illumination.

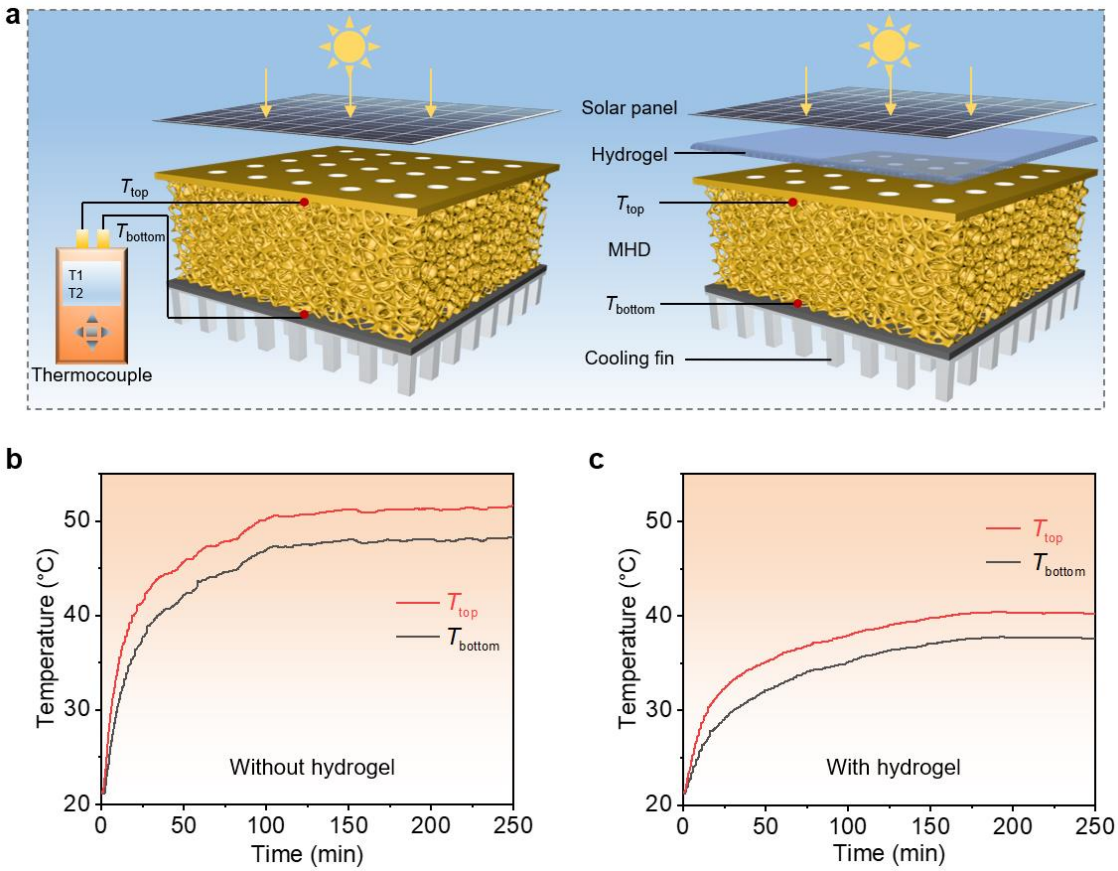

Figure S23. Temperature characterization of the MHD. (a) Schematic of the experimental setup for measuring the top and bottom surface temperatures of the MHD beneath the PV panel without (left) and with the hydrogel cooling layer (right) under one-sun illumination. (b, c) Temperature variations of the top (red curve) and bottom (gray curve) surfaces of the MHD beneath the PV panel with (b) and without the hydrogel cooling layer (c) under one-sun illumination. The top surface temperature reaches 50 °C without the hydrogel cooling layer, whereas it remains below 40 °C with the hydrogel cooling layer. The hydrogel layer supplies moisture to the MHD and reduces its surface temperature, preventing rapid water loss due to overheating of the PV panel.

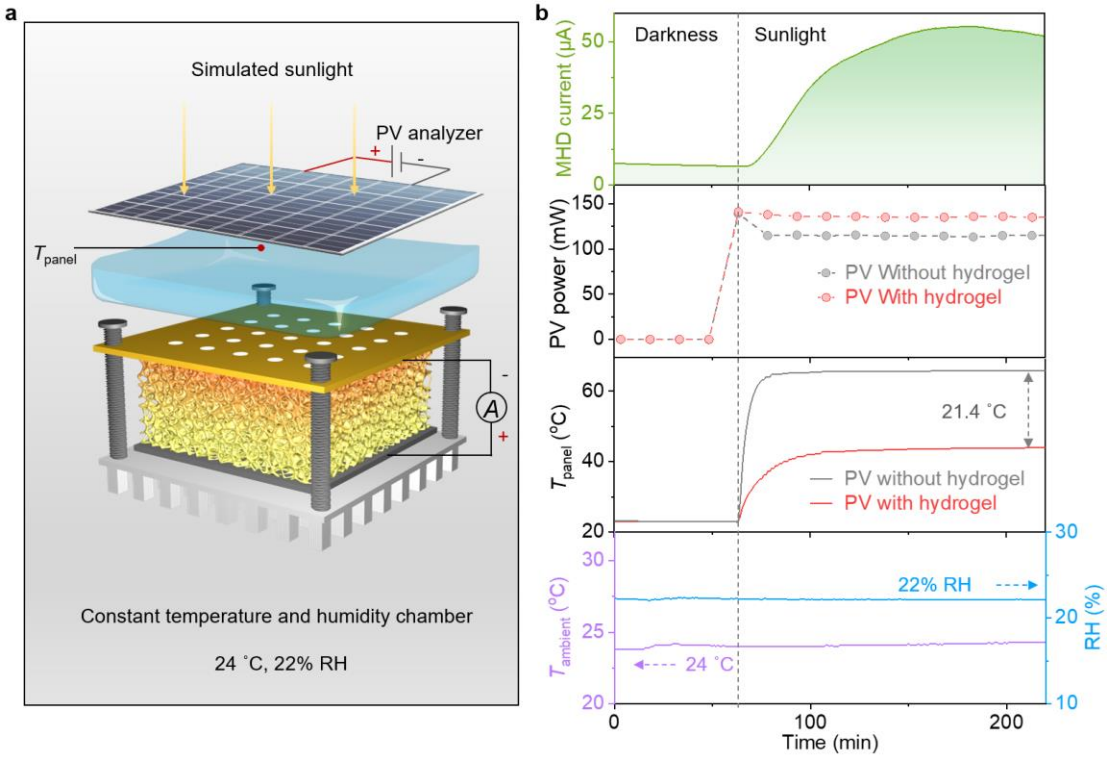

Figure S24. Performance of the PV–hydrogel–MHD system under controlled indoor low-humidity environment. (a) Schematic illustration of the experimental setup. The integrated system was placed inside a constant temperature–humidity chamber (~24°C; ~22% RH). A solar simulator (1000 W m^{-2}) was used to illuminate this system. The MHD current, PV electrical power, PV temperature, and ambient temperature/RH inside the chamber were recorded simultaneously. (b) Time-resolved output characteristics under one-sun illumination. From top to bottom: MHD current (green), initially low due to limited ambient moisture and gradually increasing under solar illumination; output power of PV panels with hydrogel (red) and without hydrogel (gray); temperature variation of PV panels with hydrogel (red) and without hydrogel (gray); ambient temperature (purple) and relative humidity (blue) inside the chamber. These results demonstrate that the integrated system operates effectively under low-humidity indoor conditions.

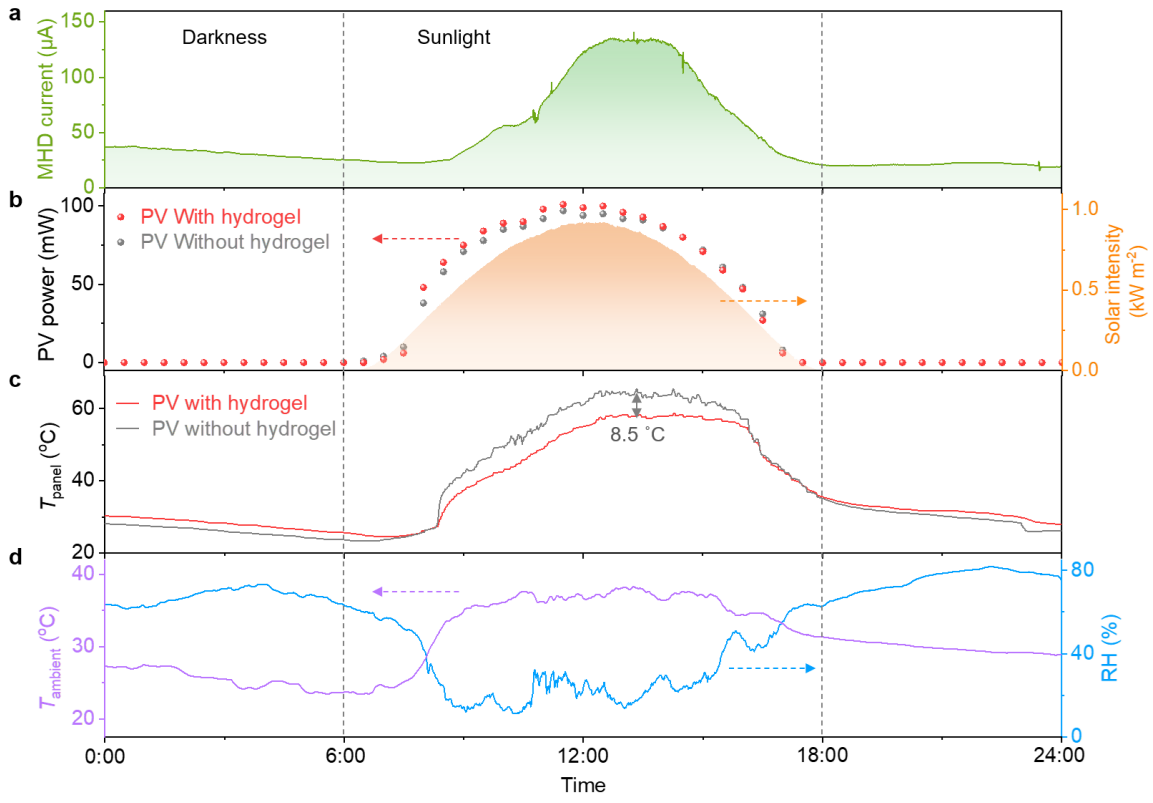

Figure S25. Outdoor performance of the system in an arid climate (Jeddah, Saudi Arabia). (a) Time-resolved MHD current over a full 24 h cycle. The current increases from ~25 μA to a peak of ~134 μA under solar illumination. (b) Electrical output power of PV panels with hydrogel (red) and without hydrogel (gray), plotted together with real-time solar intensity (orange, right axis). The hydrogel-cooled PV exhibits an average power enhancement of ~5 % throughout daytime operation. (c) Temperature variation of PV panels with (red) and without hydrogel (gray). The hydrogel-coated PV panel remains ~8.5 °C cooler than the uncooled control during peak sunlight. (d) Ambient temperature (purple) and relative humidity (blue) during the outdoor test. The daytime temperature reaches ~38 °C, while RH drops to a minimum of ~11.2 %, characteristic of a hot–arid desert environment. These results demonstrate that the PV–hydrogel–MHD system maintains effective thermal regulation and continuous hydrovoltaic electricity generation under extremely low-humidity and high-temperature conditions typical of sun-rich arid regions.

Note S1. Theoretical analysis of the energy balance of the system.

To rationalize the measured PV temperature evolution and cooling performance, we developed a coupled heat- and mass-transfer model for the PV–hydrogel system under outdoor operation (Fig. S26). The model is evaluated at a representative quasi-steady noon condition, where ambient temperature, relative humidity, and PV operating temperature are taken directly from outdoor measurements, while the associated heat-flux partitioning is obtained from the model.

Bare PV system: As shown in Figure S26a, the steady-state heat balance of the bare PV system can be expressed as:[5]

$$P_{\mathrm{solar}} = P_{\mathrm{rad,net}} + P_{\mathrm{PV,air}}^{\mathrm{conv}} + P_{\mathrm{PV}} \quad (1)$$

where P_{solar} is the absorbed solar power by the PV panel, $P_{\mathrm{rad,net}}$ is the net radiative heat exchange between the PV and sky/atmosphere, $P_{\mathrm{PV,air}}^{\mathrm{conv}}$ is the convective heat transfer path between PV and air, and P_{PV} is the electrical output of the PV panel.

The absorbed solar power P_{solar} is expressed as:[6]

$$P_{\mathrm{solar}} = \alpha S_{\mathrm{solar}} \quad (2)$$

where α is the solar absorptance of the PV panel (i.e., 0.9), and S_{solar} is the solar irradiance (1000 W m^{-2}).

The net long-wave radiation $P_{\mathrm{rad,net}}$ can be expressed as:[5]

$$P_{\mathrm{rad,net}} = \varepsilon_{\mathrm{s}}\sigma(T_{\mathrm{PV}}^4 - \varepsilon_{\mathrm{atm}}T_{\mathrm{amb}}^4) \quad (3)$$

where ε_{s} is the long-wave emissivity of the PV panel (i.e., 0.95), σ is Stefan-Boltzmann constant (i.e., 5.67×10^{-8} W m^{-2} K^{-4}), and T_{PV} and T_{amb} are the absolute temperatures of the PV surface and the ambient air, respectively. $\varepsilon_{\mathrm{atm}}$ is the effective atmospheric emissivity, which can be empirically calculated through dew point:[7]

$$\varepsilon_{\mathrm{atm}} = 0.711 + 0.0056T_{\mathrm{dew}} + 7.3 \times 10^{-5}T_{\mathrm{dew}}^2 \quad (4)$$

where T_{dew} is the dew point temperature (°C). Figure S26b illustrates the corresponding heat-resistance framework, with all energy pathways explicitly labeled.

PV–hydrogel–MHD system: To clarify all heat transfer pathways in the PV–hydrogel–MHD system, we constructed a steady-state energy network consisting of six nodes: solar, PV, hydrogel, MHD, ambient air, and sky/universe (Figure S26c). Energy balances of are as follows:

PV panel:

$$P_{\mathrm{solar}} = P_{\mathrm{rad,net}} + P_{\mathrm{PV,air}}^{\mathrm{conv}} + P_{\mathrm{PV,gel}}^{\mathrm{cond}} + P_{\mathrm{PV}} \tag{5}$$

Hydrogel layer:

$$P_{\mathrm{PV,gel}} = P_{\mathrm{evap}} + P_{\mathrm{gel,air}}^{\mathrm{conv}} + P_{\mathrm{gel,MHD}}^{\mathrm{cond}} \tag{6}$$

MHD module:

$$P_{\mathrm{gel,MHD}}^{\mathrm{cond}} + P_{\mathrm{ads}}^{\mathrm{MHD}} = P_{\mathrm{MHD,air}}^{\mathrm{conv}} + P_{\mathrm{MHD}} \tag{7}$$

Here $P_{\mathrm{PV,air}}^{\mathrm{conv}}$, $P_{\mathrm{PV,gel}}^{\mathrm{cond}}$, $P_{\mathrm{gel,air}}^{\mathrm{conv}}$, $P_{\mathrm{gel,MHD}}^{\mathrm{cond}}$, and $P_{\mathrm{MHD,air}}^{\mathrm{conv}}$ correspond to the convective or conductive heat transfer paths between PV and air, PV and hydrogel, hydrogel and air, hydrogel and MHD, and MHD and air, respectively; P_{evap} is the evaporative latent-heat removal by the hydrogel; $P_{\mathrm{ads}}^{\mathrm{MHD}}$ is the vapor-adsorption heat at the MHD interface; and P_{MHD} is the electrical output of the MHD.

Convection terms $P_{\mathrm{PV,air}}^{\mathrm{conv}}$, $P_{\mathrm{gel,air}}^{\mathrm{conv}}$, and $P_{\mathrm{MHD,air}}^{\mathrm{conv}}$ can be expressed as:[8]

$$P_{\mathrm{PV,air}}^{\mathrm{conv}} = h_{\mathrm{conv}}(T_{\mathrm{PV}} - T_{\mathrm{amb}}) \tag{8}$$

$$P_{\mathrm{gel,air}}^{\mathrm{conv}} = h_{\mathrm{conv}}\left(T_{\mathrm{gel}} - T_{\mathrm{amb}}\right) \tag{9}$$

$$P_{\mathrm{MHD,air}}^{\mathrm{conv}} = h_{\mathrm{conv}}(T_{\mathrm{MHD}} - T_{\mathrm{amb}}) \tag{10}$$

where T_{gel} and T_{MHD} are the temperatures of the hydrogel and MHD, respectively. The convective heat transfer coefficient h_{conv} can be empirically calculated as:[9]

$$h_{\mathrm{conv}} = 5.7 + 3.8\,V\ (\mathrm{W\,m^{-2}\,K^{-1}}) \tag{11}$$

where V is the wind speed (m $\mathrm{s^{-1}}$).

Conduction terms $P_{\mathrm{PV,gel}}^{\mathrm{cond}}$ and $P_{\mathrm{gel,MHD}}^{\mathrm{cond}}$ can be expressed as:[8]

$$P_{\mathrm{PV,gel}}^{\mathrm{cond}} = \frac{T_{\mathrm{PV}} - T_{\mathrm{gel}}}{R_{\mathrm{PV,gel}}} \tag{12}$$

$$P_{\mathrm{gel,MHD}}^{\mathrm{cond}} = \frac{T_{\mathrm{gel}} - T_{\mathrm{MHD}}}{R_{\mathrm{gel,MHD}}} \tag{13}$$

where $R_{\mathrm{PV,gel}}$ ($\mathrm{m^2\,K\,W^{-1}}$) is the thermal contact resistance between PV and hydrogel and $R_{\mathrm{gel,MHD}}$ is the thermal contact resistance between hydrogel and MHD. The conductive contact resistance R can be modeled by a series-layer scheme $R = \sum t_i/k_i$, where t and k represent the thickness and thermal conductivity of each component.[8, 10] For the PV–hydrogel interface, we

considered the PV backsheet (PET/EVA, $t_1 \approx 0.5$ mm, $k_1 \approx 0.3$ W m^{-1} K^{-1}) and the hydrogel layer ($t_2 \approx 8$ mm, $k_2 \approx 0.51$ W m^{-1} K^{-1}), giving $R_{\mathrm{PV,gel}} \approx 0.017$ m^2 K W^{-1}. For the hydrogel–MHD pathway, the two layers are separated by an open, ventilated gap where only a small fraction of the area is in direct solid contact. Treating this as parallel contributions of sparse solid supports and air conduction/radiation yields a $R_{\mathrm{gel,MHD}} \approx 3$ m^2 K W^{-1},[8, 10] indicating weak thermal coupling between the hydrogel and the MHD module, so the majority of the heat extracted from the PV is released via evaporation and convection.

P_{evap} can be expressed as:[11]

$$P_{\mathrm{evap}} = \frac{\Delta H_{\mathrm{evap}} \Delta m}{tA} \tag{14}$$

where ΔH_{evap} is the hydrogel evaporation enthalpy, Δm is the mass change of the hydrogel layer due to water evaporation loss, t is the test time, and A is the surface area of the hydrogel.

$P_{\mathrm{ads}}^{\mathrm{MHD}}$ can be expressed as:

$$P_{\mathrm{ads}}^{\mathrm{MHD}} = (1 - f) P_{\mathrm{evap}} \tag{15}$$

where f is the fraction of vapor going to air (i.e. $f \approx 0.98$). Since only a small fraction (~2 %) of the evaporated vapor is adsorbed by the MHD, $P_{\mathrm{ads}}^{\mathrm{MHD}}$ is neglected in the hydrogel energy balance but retained in the MHD balance for completeness. The corresponding energy flow of the PV–hydrogel–MHD system is illustrated in Figure S26d.

We further performed COMSOL Multiphysics simulations of the PV module with and without the hydrogel layer. The simulations show that the hydrogel-cooled PV stabilizes at ~55 °C, exhibiting a temperature reduction of ~12 °C relative to the bare module (Figure S27a), in good agreement with the infrared thermal images (Figure S27b). These theoretical and numerical results corroborate our experiments and clearly demonstrate that incorporating the hydrogel–MHD system introduces a robust, dominant evaporative cooling channel that actively enhances PV cooling.

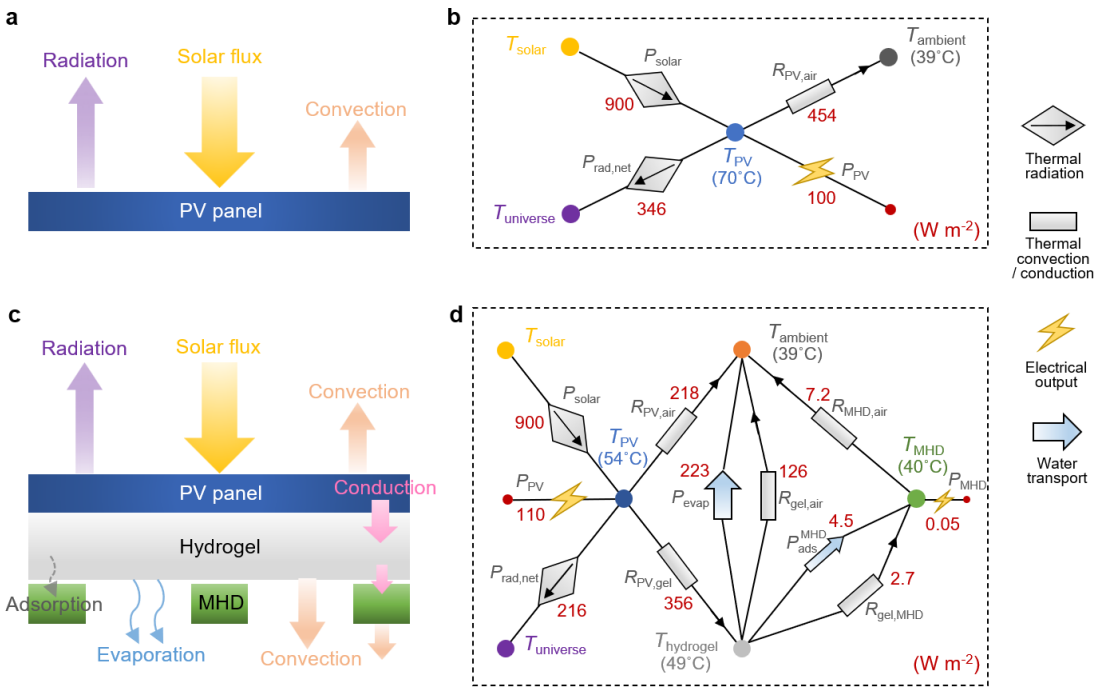

Figure S26. Steady-state heat transfer in the bare PV and hybrid PV–hydrogel–MHD system under solar irradiation. (a) In the bare PV system, the PV panel absorbs solar irradiation and dissipates heat via thermal radiation to the sky and convection to ambient air. (b) Energy flow diagram showing the steady-state thermal pathways among the PV panel, ambient air, and outer space. P_{solar} is the absorbed solar energy by the PV panel; P_{PV} is the electrical output of the PV panel; $P_{rad,net}$ is the net radiative heat exchange between the PV and the sky/universe. $R_{PV,gel}$ denotes the thermal resistance corresponding to convection between PV and air. (c) In the PV–hydrogel–MHD system, the PV panel dissipates heat via thermal radiation to the sky, convection to ambient air, and conduction into the underlying hydrogel. The hydrogel cools the PV by evaporating water into the surrounding air. A small fraction of the generated water vapor is adsorbed by the MHD modules, which produces electricity. (d) Energy flow diagram showing the steady-state thermal and mass transport pathways among the PV panel, hydrogel layer, MHD modules, ambient air, and outer space. $\boldsymbol{P_{MHD}}$ is the electrical output of the MHD. P_{evap} represents the evaporative cooling power of the hydrogel, while $\boldsymbol{P^{MHD}_{ads}}$ denotes the vapor adsorption heat at the MHD interface. $R_{PV,air}$, $R_{PV,gel}$, $R_{gel,air}$, $R_{gel,MHD}$, and $R_{MHD,air}$ denote thermal resistances corresponding to convection or conduction between PV and air, PV and hydrogel, hydrogel and air, hydrogel and MHD, and MHD and air, respectively. Arrows indicate the direction of heat or moisture transport. All heat fluxes are expressed per unit area (W m^{-2}).

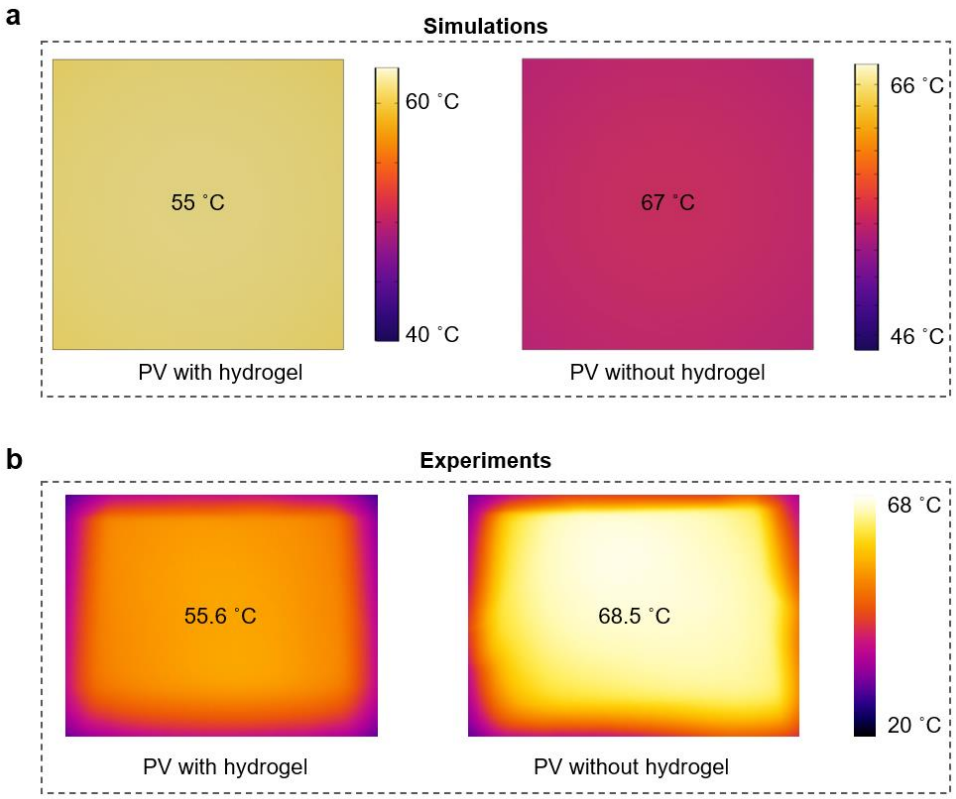

Figure S27. Numerical and experimental validation of PV cooling by the hydrogel layer. (a) Simulated temperature distribution of the PV with hydrogel cooling layer (left) and the bare PV module (right). (b) Infrared thermal image of the PV with hydrogel cooling layer (left) and the bare PV module (right). The temperature is labeled at the center of the image.

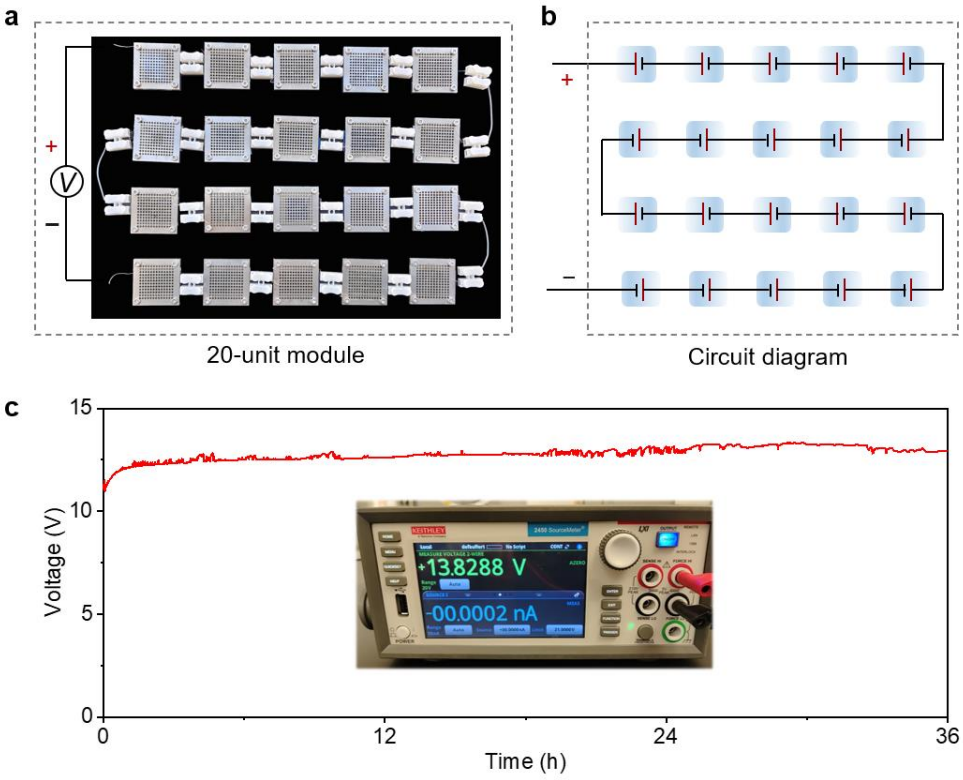

Figure S28. Output voltage of a 20-unit module connected in series. (a) Photograph of the integrated array containing 20 MHDs. (b) Circuit diagram of the integrated array of 20 MHDs. (c) Recorded voltage of the integrated array. The total output voltage of the module reaches up to 13 V and is sustained for over 36 h.

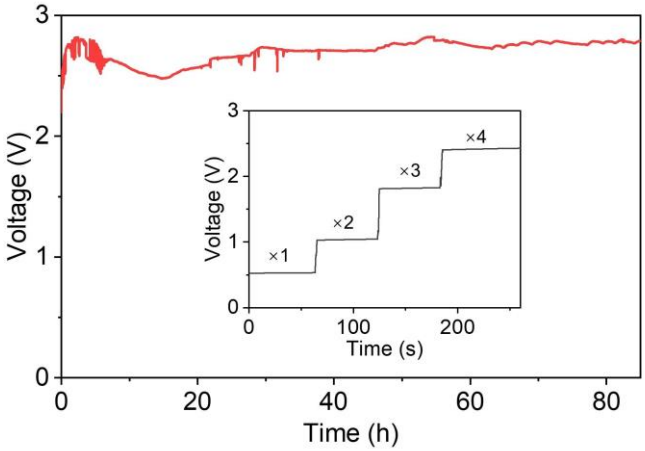

Figure S29. Output voltage of a module containing four MHD cells connected in series. The inset shows the total voltage variation as the number of modules increases from one to four.

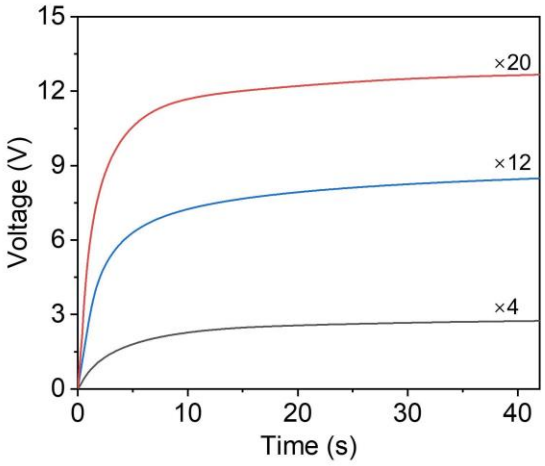

Figure S30. Voltage–time curves of a commercial capacitor (47 μF) charged by serial MHD modules containing 4, 12, and 20 units. The output voltage can be tuned by adjusting the number of modules connected in series.

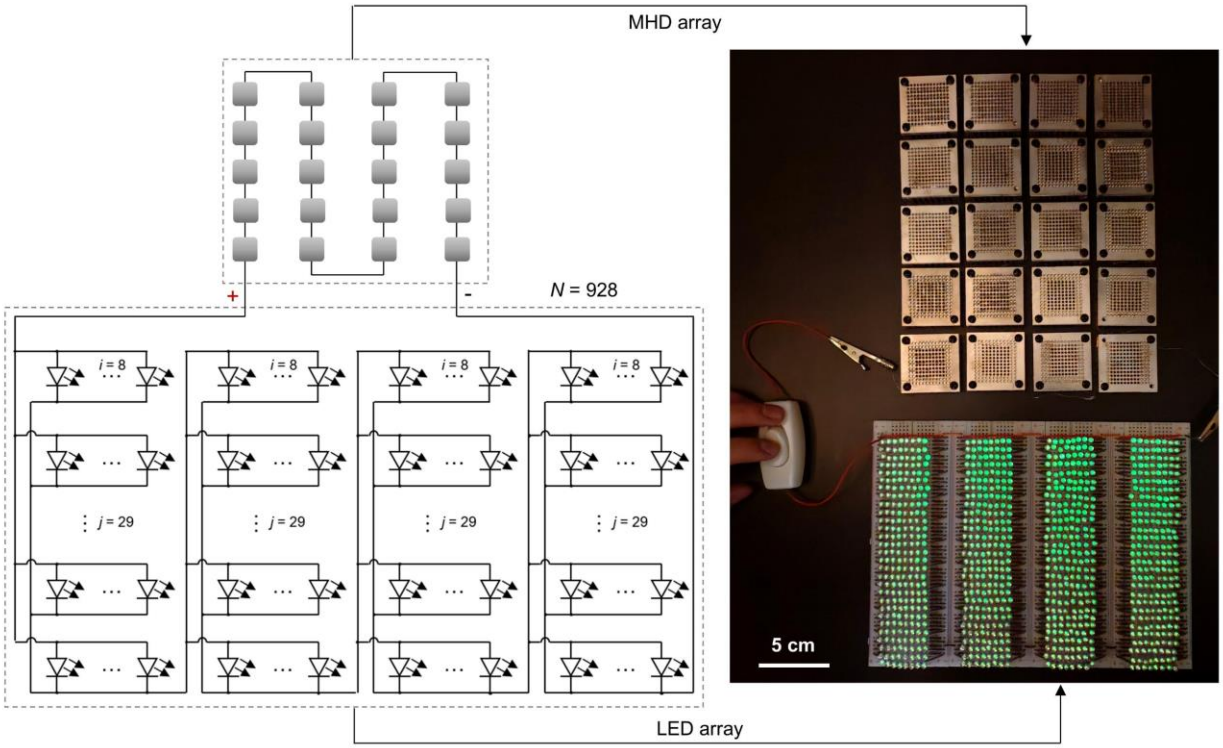

Figure S31. Schematic of the circuit design and demonstration of LED array powering. The circuit consists of four groups of LED arrays connected in series, with each group containing 232 LEDs connected in parallel. The LED arrays can be directly powered by a 20-unit MHD array connected in series (right panel).

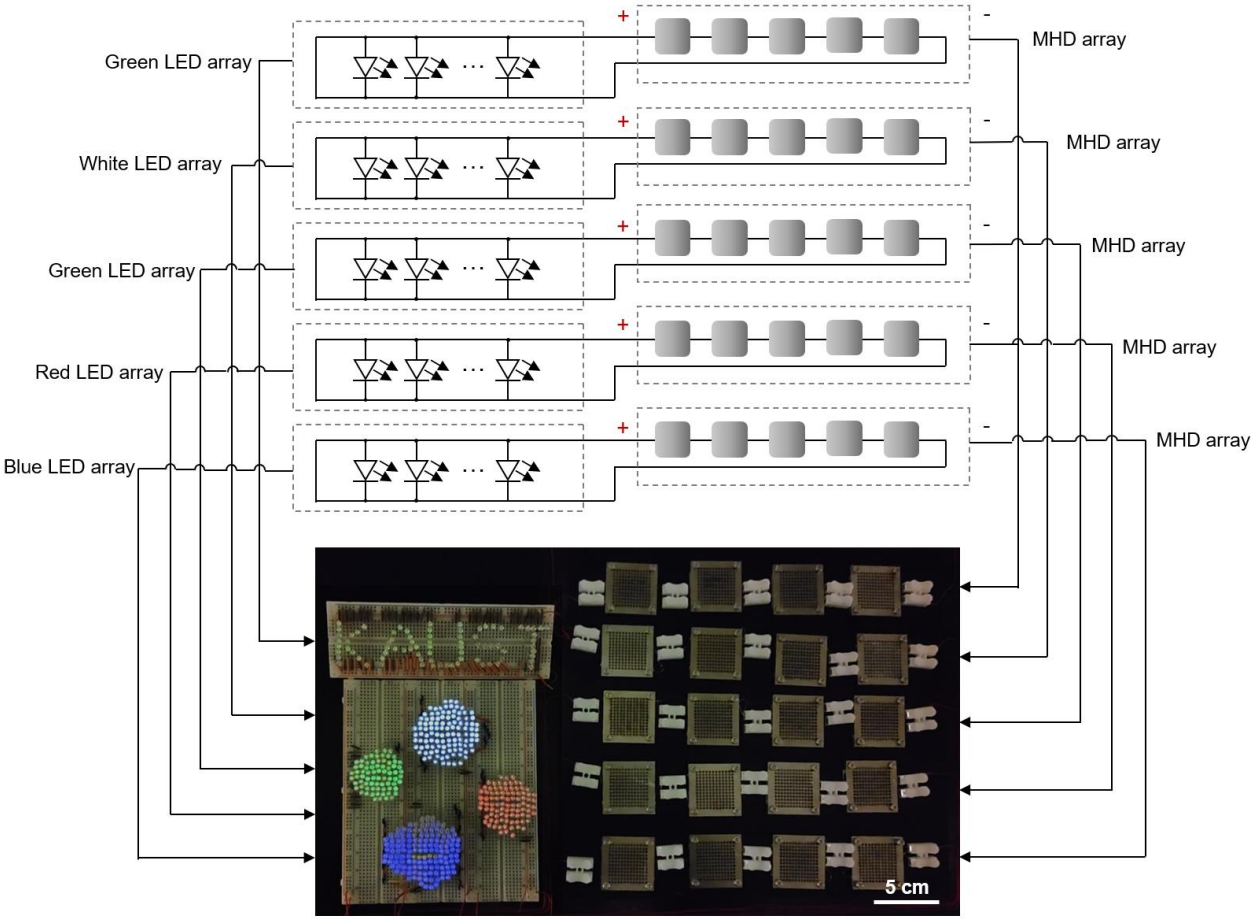

Figure S32. Schematic of the circuit design and demonstration of a complex LED pattern powering. The circuit consists of five groups of LED arrays, with each group containing LEDs of the same color. Each group is powered by a four-unit MHD module (bottom panel).

Table S1.

Comparison of representative MHD systems with the present work. It is worth noting that the comparison focuses on systems employing inert electrodes (e.g., Au, graphite, carbon) to ensure a fair assessment of hydrovoltaic performance, excluding devices that rely on active metal electrodes where redox reactions contribute significantly to the output.

Materials	Power density ($mW\ m^{-2}$)	Voltage (V)	Current ($\mu A\ cm^{-2}$)	Duration	Electrode	Ref
GO	20.2	0.45	4.45	500 s	Au	[12]
GO/PAAS	0.7	0.6	1	120 h	Au/Ag	[13]
PSSA	170	0.8	100	1400 s	Carbon	[14]
Cellulose	0.003	0.11	22	~10 h	Pt	[15]
PSSA/PDDA	0.056	1.38	0.06	250 h	Carbon tape	[16]
SA/SiO_2/rGO	120	0.6	122	~4 h	Au	[17]
Cellulose/CB	6.5	0.75	0.86	240 h	Carbon tape	[18]
Nafion/pNIPAm	101.4	1.86	25	600 s	Carbon paper	[19]
Wood	5.68	0.57	77	28 h	Pt	[20]
H-PSS	130	0.8	120	12 h	Au	[1]
PSSA-PEDOT:PSS-$FeCN^{4-/3-}$	60	0.86	130	25 h	Graphite	[21]
Protein	116	1.45	113	~4 h	FTO/CNT	[22]
Gradient-BP hydrogel	0.1	0.25	0.16	3000 s	Carbon cloth	[23]
Cellulose/PSSA/ H_2SO_4/PEDOT:PSS/$K_3[Fe(CN)_6]$/ $K_4[Fe(CN)_6]$	20	0.7	25	750 h	Au/ graphite	This work

Table S2.

Comparison of steady-state temperature and output power of PV panels with different cooling strategies under one-sun illumination.

Cooling type	Temperature (°C)	Output power (W)
Bare PV panel	69.2	0.388
PV + cooling fin	60.5	0.409
PV + hydrogel	55.7	0.432
PV + hydrogel + cooling fin	58.9	0.413

Table S3.

Performance comparison of representative sorbent-based PV thermal management systems and the developed hydrogel–MHD system in this work.

Materials	Temperature reduction (°C)	Cooling power (W m^{-2})	PV power improvement (%)	Ref.
PAM-CNT-$CaCl_2$ hydrogel	10	295	5	[11]
Pam/alginate-$CaCl_2$ hydrogel	6.4	~140	~3.3	[24]
ACC/PAA/PEGhydrogel	5	70	0.06	[25]
Li-PAAm hydrogel	17	159	6.9	[26]
LiCl@ACFF	9.7	356	3.4	[27]
KC/PPy/LiCl beads	10	298	3.9	[28]
PAM-carbon black hydrogel	9.9	288	5.9	[29]
MOF-coated heat sink	~10	106	6.8	[30]
PAAS/LiCl	13.5	302–408	15	This work

Table S4.

Cost analysis of the system. All prices are based on bulk market quotations (Alibaba, Thermo Fisher Scientific, Aladdin Scientific, etc.).

Category	Component	Materials	Unit price ($ kg^{-1})	Amount (kg m^{-2})	Cost ($ m^{-2})	Supplier
MHD module (36.8 $ m^{-2})	Power-generating layer	Cellulose film	2.1	0.450	0.9	Alibaba
		PSSA solution (30 wt%)	10	0.493	4.9	Alibaba
		H_2SO_4 (5 wt%)	13.4	0.493	6.6	Thermo Fisher
		PEDOT:PSS	22	0.088	1.9	Alibaba
		$K_3[Fe(CN)_6]$	44.1	0.011	0.5	Aladdin
		$K_4[Fe(CN)_6]$	44.1	0.011	0.5	Aladdin
	Electrodes	Graphite foil	6.5	1.8	11.7	Alibaba
		Stainless steel	2.5	3.9	9.8	Alibaba
Hydrogel cooling layer (18.2 $ m^{-2})	Hydrogel	PAAS	4.15	2.5	10.4	Alibaba
		LiCl	4.66	1.3	6.1	Alibaba
		Deionized water	0.9	1.9	1.7	Millipore
Others (20.2 $ m^{-2})	Cooling fin	Aluminum cooling fin	4.5	2.7	12.2	Alibaba
	Mechanical fixtures	Plastic bolts / supports	0.005 $ pc^{-1}	1600 pcs m^{-2}	8	Alibaba
Total system	—	—	—	—	75.2	—

References and Notes

1. Y. Huang, K. Zhou, H. Cheng, T. He, H. Wang, J. Bai, C. Yang, T. Guang, H. Yao, F. Li, G. Hou, Z. Xu and L. Qu, *Adv. Funct. Mater.*, 2024, **34**, 2308620.
2. S. Yang, L. Zhang, J. Mao, J. Guo, Y. Chai, J. Hao, W. Chen and X. Tao, *Nat. Commun.*, 2024, **15**, 3329.
3. C. D. Díaz-Marín, Massachusetts Institute of Technology, 2024.
4. H. Fang, S. Dang, P. Kumar, J. Wang, L. Xu, Y. Zhu, A. Almogbel, A. Albadri, S. De Wolf and Q. Gan, *Mater. Sci. Eng. R Rep.*, 2025, **165**, 101016.
5. T. Li, M. Wu, J. Xu, R. Du, T. Yan, P. Wang, Z. Bai, R. Wang and S. Wang, *Nat. Commun.*, 2022, **13**, 6771.
6. J. Xu, X. Huo, T. Yan, P. Wang, Z. Bai, J. Chao, R. Yang, R. Wang and T. Li, *Energy Environ. Sci*, 2024, **17**, 4988-5001.
7. M. Martin and P. Berdahl, *Sol. Energy*, 1984, **32**, 663-664.
8. T. L. Bergman, *Fundamentals of heat and mass transfer*, John Wiley & Sons, 2011.
9. J. Palyvos, *Appl. Therm. Eng.*, 2008, **28**, 801-808.
10. W. M. Rohsenow, J. P. Hartnett and Y. I. Cho, *Handbook of heat transfer*, Mcgraw-hill New York, 1998.
11. R. Li, Y. Shi, M. Wu, S. Hong and P. Wang, *Nat. Sustainability*, 2020, **3**, 636-643.
12. H. Cheng, Y. Huang, F. Zhao, C. Yang, P. Zhang, L. Jiang, G. Shi and L. Qu, *Energy Environ. Sci*, 2018, **11**, 2839-2845.
13. Y. Huang, H. Cheng, C. Yang, H. Yao, C. Li and L. Qu, *Energy Environ. Sci*, 2019, **12**, 1848-1856.
14. T. Xu, X. Ding, Y. Huang, C. Shao, L. Song, X. Gao, Z. Zhang and L. Qu, *Energy Environ. Sci*, 2019, **12**, 972-978.
15. M. Li, L. Zong, W. Yang, X. Li, J. You, X. Wu, Z. Li and C. Li, *Adv. Funct. Mater.*, 2019, **29**, 1901798.
16. H. Wang, Y. Sun, T. He, Y. Huang, H. Cheng, C. Li, D. Xie, P. Yang, Y. Zhang and L. Qu, *Nat. Nanotechnol.*, 2021, **16**, 811-819.
17. H. Wang, T. He, X. Hao, Y. Huang, H. Yao, F. Liu, H. Cheng and L. Qu, *Nat. Commun.*, 2022, **13**, 2524.

18. J. Tan, S. Fang, Z. Zhang, J. Yin, L. Li, X. Wang and W. Guo, *Nat. Commun.*, 2022, **13**, 3643.
19. C. Liu, S. Wang, X. Wang, J. Mao, Y. Chen, N. Fang and S.-P. Feng, *Energy Environ. Sci*, 2022, **15**, 2489-2498.
20. T. Cai, L. Lan, B. Peng, C. Zhang, S. Dai, C. Zhang, J. Ping and Y. Ying, *Nano Lett.*, 2022, **22**, 6476-6483.
21. J. Bai, Y. Hu, T. Guang, K. Zhu, H. Wang, H. Cheng, F. Liu and L. Qu, *Energy Environ. Sci*, 2022, **15**, 3086-3096.
22. R. Zhu, Y. Zhu, L. Hu, P. Guan, D. Su, S. Zhang, C. Liu, Z. Feng, G. Hu, F. Chen, T. Wan, X. Guan, T. Wu, R. Joshi, M. Li, C. Cazorla, Y. Lu, Z. Han, H. Xu and D. Chu, *Energy Environ. Sci*, 2023, **16**, 2338-2345.
23. J. Liang, Y. Wang, X. Ma, X. Song, H. Wang, T. Shen, J. Sun, Y. Hu, Y. Liu, Z. Wu, T. Yu, Z. Tie and Z. Jin, *Adv. Funct. Mater.*, 2025, **35**, 2418834.
24. Z. Li, T. Ma, F. Ji, H. Shan, Y. Dai and R. Wang, *ACS Energy Lett.*, 2023, **8**, 1921-1928.
25. T. Lv, L. Sun, Y. Yang and J. Huang, *Sol. Energy*, 2021, **216**, 358-364.
26. S. Pu, J. Fu, Y. Liao, L. Ge, Y. Zhou, S. Zhang, S. Zhao, X. Liu, X. Hu, K. Liu and J. Chen, *Adv. Mater.*, 2020, **32**, 1907307.
27. J. Cai, W. Li, S. Jin, L. Shen, B. Wang, Z. Gan, Q. Pan and X. Zheng, *Renew. Energy*, 2024, **237**, 121805.
28. J. He, N. Li, S. Wang, S. Li, C. Wang, L. Yu, P. Murto and X. Xu, *J. Mater. Chem. A*, 2022, **10**, 8556-8567.
29. Y. Liu, Z. Liu, Z. Wang, W. Sun and F. Kong, *Appl. Therm. Eng.*, 2024, **240**, 122185.
30. D. Alezi, R. Li, N. Alsadun, A. Malik, O. Shekhah, P. Wang and M. Eddaoudi, *Mater. Adv.*, 2024, **5**, 4660-4667.